



Incorporation of Functionalized Calcium Phosphate Nanoparticles in Living Cells

Manuel Rivas¹ · Pau Turon² · Carlos Alemán¹ · Jordi Puiggali¹ · Luis J. del Valle¹

Received: 14 July 2021 / Accepted: 17 September 2021

© The Author(s) 2021

Abstract

Intracellular calcium (Ca^{2+}) is a key signaling element that is involved in a great variety of fundamental biological processes. Thus, Ca^{2+} deregulation would be involved in the cancer cell progression and damage of mitochondrial membrane and DNA, which lead to apoptosis and necrosis. In this study, we have prepared amorphous calcium phosphate nanoparticles (ACP NPs) for studied their incorporation by endocytosis or electroporation to epithelial, endothelial and fibroblast cells (MCF-7, HUVEC and COS-1 cells, respectively). Our results showed that internalized ACP NPs have cytotoxic effects as a consequence of the increase of the intracellular calcium content. The endocytosis pathways showed a greater cytotoxic effect since calcium ions could easily be released from the nanoparticles and be accumulated in the lysosomes and mitochondria. In addition, the cytotoxic effect could be reversed when calcium ion was chelated with ethylene glycol-bis(2-aminoethylether)-N,N,N',N'-tetraacetic acid (EGTA). Modification of ACP NPs by coating with different compounds based on phosphates was also evaluated. The results indicated a reduction of the cytotoxic effect, in the order polyphosphate < phosphonic acid < orthophosphate. A differential cytotoxic effect of ACP-NPs was observed in function of the cell type; the cytotoxic effect can be ordered as i.e., HUVEC > COS-1 > MCF-7. The greater cytotoxic effect caused by the increase of intracellular calcium that is observed in normal cells and the greater resistance of cancer cells suggests new perspectives for cancer research.

Keywords Amorphous calcium phosphate · Nanoparticles · Cytotoxic effect · Cancer · Intracellular calcium

Introduction

Calcium (Ca^{2+}) is a key signaling element that is involved in a great variety of fundamental biological processes (e.g. from fertilization to programmed cell death). Thus, almost every tissue and biofluid has specific functions that are controlled by Ca^{2+} [1]. Besides, calcium is the most abundant metallic element in the body, being adequate intake amounts (1.0–1.2 g/day) obtained from dairy

products and some green vegetables. However, calcium has recently been associated with some risk of cancer. For example, colorectal cancer [2–4], accumulation of calcium in the peripheral zone of human prostate gland could play an important role in the prostate cancer [5].

Calcium deregulation has extensively been studied at cellular and molecular levels due to its clear effect on cell injury, carcinogenesis and cell death [6, 7]. For instance, Ca^{2+} can activate transcription factors, such as nuclear factor of activated T cells (NFAT) [6], regulate cell proliferation promoting cancer cell progression [8], modulate poly-ADP-ribose polymerase, permeabilization of mitochondrial membrane and DNA damage leading to apoptosis and necrosis [9].

Calcium is also a key regulator of the mitochondrial function and acts at several levels within the organelle to stimulate ATP synthesis. Deregulation of mitochondrial [Ca^{2+}] homeostasis is now recognized to play a key role in several pathologies (e.g. enhanced generation of reactive oxygen species (ROS), release of cytochrome C, and

✉ Jordi Puiggali
jordi.puiggali@upc.edu

✉ Luis J. del Valle
luis.javier.del.valle@upc.edu

¹ Departament d'Enginyeria Química and Barcelona Research Center for Multiscale Science and Engineering EEBE, Universitat Politècnica de Catalunya, Av. Eduard Maristany 16, 08019 Barcelona, Spain

² B. Braun Surgical, S.A., Carretera de Terrassa 121, 08191 Rubí, Barcelona, Spain

alteration of the activity of the mitochondrial permeability transition pore) [10], which can lead again to apoptosis and necrosis [11].

It has recently been suggested that cancer cells may have a mitochondrial dysfunction, being adapted to aerobic glycolysis in order to generate ATP. The signaling role of ROS has been recognized [12]. Recent studies suggest that cancer cells, compared with normal cells, undergo an increased oxidative stress that can be associated with oncogenic transformation, alterations in metabolic activity, and increased generation of ROS [13]. In turn, the increased ROS in cancer cells may affect certain redox-sensitive molecules and further lead to significant consequences, such as stimulation of cellular proliferation, cell differentiation, alterations in sensitivity to anticancer agents, promotion of mutations and genetic instability, and contribution to carcinogenesis [13]. Perturbation of mitochondrial respiration in cancer cells leads to redox alterations and highly invasive behaviors, which seem to be mediated by elevated cytosolic calcium [14].

Until recently, necrosis, unlike apoptosis, was considered as passive and unregulated form of cell death. However, during the last decade a number of experimental data demonstrated that, except under extreme conditions, necrosis may be a well-regulated process activated by rather specific physiological and pathological stimuli [15]. Proskuryakov et al. have considered mechanisms and the role of necrosis in tumor cells [16]. Mitochondrial collapse activates various proteases (e.g. calpains and cathepsin) and phospholipases, and eventually leads to plasma membrane destruction, a hallmark of necrotic cell death. Necrosis, in contrast to apoptosis, usually evokes powerful inflammatory response, which may participate in tumor regression during anticancer therapy. However, excessive spontaneous necrosis during tumor development may lead to more aggressive tumors due to the stimulated growth caused by the necrosis-induced inflammation [16].

In this study, we have addressed on the particular histological architecture of tumors. Willis defined a tumor (neoplasm) as a mass, the growth of which is uncoordinated with the surrounding normal tissues and persists in the absence of the inciting stimulus [17]. It is worth considering this definition in detail. First, the mass, like any other tissue, is composed of parenchymal cells and stroma, which are the essential parts of an organ. The parenchymal cells of the mass may be well differentiated, organized as normal tissues, and had a slow proliferation, or on the contrary, they may be poorly differentiated, had little or no organization and a fast proliferation. In either situation, the host response is mediated by angiogenic factors [18, 19], which are synthesized by the parenchyma of the tumor and

stimulate proliferation of all stromal cells, including fibroblasts and vascular cells.

Hydroxyapatite (HAp) nanoparticles are able to encapsulate different drugs (e.g. chloramphenicol) [20] and also to be internalized by endocytosis due to their small size. These nanoparticles are also a source of Ca^{2+} ions, which can be delivered inside cells due to their solubilization in acidic media. The released Ca^{2+} can be accumulated in lysosomes and mitochondria provoking a necrotic effect, which deserves also the attention of the present work. In this work, we explore the intracellular incorporation pathway of Ca^{2+} free and released from the calcium phosphate nanoparticles (NPs), the influence of the size being also investigated in the latter case (i.e. NPs < 200 nm and NPs > 200 nm).

Materials and Methods

Materials

Tetrasodium pyrophosphate ($\text{Na}_4\text{P}_2\text{O}_7$), sodium triphosphate (polyP), aminotris(methylenephosphonic acid) (ATMP), ammonium phosphate dibasic [$(\text{NH}_4)_2\text{HPO}_4$; purity $\geq 99.0\%$] and ammonium hydroxide solution 30% (NH_4OH ; purity: 28–30%) were purchased from Sigma-Aldrich. Calcium nitrate [$\text{Ca}(\text{NO}_3)_2$; purity $\geq 99.0\%$] was purchased from Panreac (Barcelona, Spain). Ethanol ($\text{C}_2\text{H}_5\text{OH}$; purity $\geq 99.5\%$) was obtained from Scharlab (Barcelona, Spain). HEPES was purchased from Lonza.

Cell line MCF-7 (epithelial cells from human breast adenocarcinoma) and COS-1 (fibroblast cells from green monkey kidney transformed by insertion of the SV40) were obtained from ATCC (HTB-22 and CRL-1650, respectively). Dulbeccó's Modified Eagle's Medium (DMEM) and Ca^{2+} -free DMEM, Fetal Bovine Serum (FBS), penicillin/streptomycin (pen/strep) and L-glutamine were purchased from Gibco. Cell line HUVEC (endothelial cells from normal human umbilical vein) (CC-2517) and EGM-2 Bulletkit with and without Ca^{2+} media optimized for certain HUVECs were purchased from Lonza. Poly-L-lysine was purchased from Merck Millipore (Germany).

Fura-2AM, Alamar blue reagent and ethylene glycol-bis(2-aminoethylether)-N,N',N'-tetra(acetoxymethyl ester) (EGTA-AM) were purchased from Invitrogen (Invitrogen-Molecular Probes, Leiden, The Netherlands). MTT solution [3-(4,5-dimethylthiazol-2-yl)-2,5-diphenyltetrazolium bromide] was purchased from Roche. Texas red dextran (MW 10,000 g/mol); and both enzymes, trypsin-EDTA solution (0.05% trypsin, 0.02% EDTA) and soluble alkaline phosphatase (10 units/mL) from bovine intestinal

mucosa were purchased from Sigma-Aldrich. Electroporation cuvettes were purchased from Molecular BioProducts Inc.

Synthesis of Amorphous Calcium Phosphate (ACP)

Amorphous calcium phosphate nanoparticles (ACP-NPs) have been considered for this study. The reagent conditions were adjusted to get a Ca/P ratio of 1.67. Specifically, 15 mL of 0.5 M $(\text{NH}_4)_2\text{HPO}_4$ in milli-Q water (pH 11 adjusted with ammonium hydroxide 30% w/v solution) were drop-wise added (rate of 2 mL/min or less) under agitation (400 rpm) to 25 mL of a 0.5 M $\text{Ca}(\text{NO}_3)_2$ ethanol solution. The reaction mixture was stirred during 1 h (400 rpm at room temperature). The reagents and the reaction were made in plastic containers to avoid the use of borosilicate glasses. Then, the resultant suspension of NPs was aged for 24 h at 37 °C. The precipitate was separated by centrifugation and washed sequentially with milli-Q water and a 60/40 v/v mixture of ethanol–water (twice). A white powder was obtained after freeze-drying.

Size Separation of NPs

The ACP-NPs were re-suspended in milli-Q water at concentration of 15 mg/mL. The procedure was performed according to BS ISO 14887 (2000) (“Sample preparation-dispersing procedures for powders in liquids”). Thus, NPs powder (300 mg) was placed in a plastic tube of 50 mL together with 10 mL of water sterile and mixed with a spatula until all visible aggregates disappeared. The wetting step was applied in order to substitute the solid-air interface by a solid-liquid interface. 10 mL of water were then added to the tube and gently mixed using a spatula. The tube was subsequently immersed in an ice bath and the sample was sonicated to ensure a complete de-agglomeration using an ultrasonic probe (Cole-Parmer® 130-Watt Ultrasonic Processors (50/60 Hz, VAC 220); product number EW-04714-51). A titanium probe of 6 mm was tuned to resonate at 20 kHz, ± 50 Hz for 20 s at 90% amplitude.

The NPs suspension was then gently mixed with a spatula rod to ensure homogeneity, and loaded in a syringe (10 mL) to be filtered through a 0.2 μm filter. Filtration was manually performed at a flow rate approximately of 1 mL/min, particles were finally concentrated using an IEC MultiRF centrifuge (Thermo IEC, Needham Heights, MA, USA). Two fractions corresponding to the eluted (i.e. NPs size < 200 nm) and retained particles (i.e. NPs with size > 200 nm) were consequently obtained.

Measurements

X-ray Diffraction

Crystallinity was studied by wide angle X-ray diffraction (WAXD). Patterns were acquired using a Bruker D8 Advance model with CuK_α radiation ($\lambda = 0.1542$ nm) and geometry of Bragg-Bretano, theta-2 theta. A one-dimensional Lynx Eye detector was employed. Samples were run at 40 kV and 40 mA, with a 2-theta range of 2–40, measurement steps of 0.02°, and time/step of 2–8 s. Diffraction profiles were processed using PeakFit v4 software (Jandel Scientific Software) and the graphical representation performed with OriginPro v8 software (OriginLab Corporation, USA).

The crystallite size (L) in the direction perpendicular to the representative (211) planes of samples was derived from the X-ray diffraction line broadening measurement using the Scherrer equation: [21]

$$L = \frac{0.9\lambda}{\beta \cos\theta} \quad (1)$$

where λ is the wavelength (CuK_α), β is the full width at half maximum height of the (211) line, θ is the diffraction angle and 0.9 is a shape factor. The crystallinity (χ_c) was obtained using the following equation [22]:

$$\chi_c = 1 - \frac{V_{112/300}}{I_{300}} \quad (2)$$

where I_{300} is the intensity of the (300) reflection and $V_{112/300}$ is the intensity of the hollow between the (112) and (300) reflections, which disappears in non-crystalline samples.

Morphological Characterization

Scanning electron microscopy (SEM) studies were carried out using a Focused Ion Beam Zeiss Neon40 microscope operating at 5 kV, equipped with an energy dispersive X-ray (EDX) spectroscopy system. Samples were deposited on a silicon disc mounted with silver paint on pin stubs of aluminum, and sputter-coated with a thin layer of carbon to prevent sample charging problems.

Adsorption of Biophosphates and Biophosphonate Onto ACP NPs < 200 nm

ACP nanoparticles were prepared and filtered using the above described procedure. After this, 500 μL of working aqueous solution (pH 7.4, adjusted with an ammonium hydroxide 30%-w/w solution), which contained 12.5 mM of polyP, $(\text{P}_2\text{O}_7)^{4-}$ or ATMP, were deposited onto 50 mg of ACP NPs < 200 nm. After overnight agitation at 25 °C,

adducts were separated by centrifugation at 6500 rpm and 4 °C during 4 min. Sediments were washed with milli-Q water for two-times. The obtained pellets were frozen at -80 °C for 3 h and lyophilized to remove the humidity. These ACP NPs were named according to their coating as NPs/polyP, NPs/(P₂O₇)⁴⁻ and NPs/ATMP. The ability of ACP to adsorb polyP, P₂O₇⁴⁻ and ATMP was determined using FTIR spectroscopy.

Some experiments were performed with nanoparticles treated with alkaline phosphatase to remove the added coating. This treatment is specific to hydrolyze the bio-phosphates in the NPs/polyP and NPs/(P₂O₇)⁴⁻ samples [23]. The uncoated NPs and NPs/ATMP were used as controls. The hydrolysis medium consisted of 10 units/mL of soluble alkaline phosphatase in 100 mM Tris-HCl buffer and 200 mM MgCl₂ at pH 7.4. The uncoated and coated NPs were incubated in this medium overnight at 37 °C under orbital agitation. Then, adducts were separated by centrifugation at 6500 rpm during 5 min. Sediments were washed with milli-Q water for two-times. Pellets were frozen at -80 °C for 3 h and lyophilized to remove the humidity. Finally, these NPs were used in electroporation (+EP) and non-electroporation (-EP) experiments as above described.

Fourier Transform Infrared (FTIR) Spectroscopy

Infrared absorption spectra were recorded with a Fourier Transform FTIR 4100 Jasco spectrometer in the 1800–700 cm⁻¹ range. A Specac model MKII Golden Gate attenuated total reflection (ATR) equipment with a heated Diamond ATR Top-Plate was used. The characteristic bands of the compounds studied in this work (substrates and adsorbed species) are listed in Table 1.

X-ray Photoelectron Spectroscopy (XPS)

XPS analyses were performed in a SPECS system equipped with a high-intensity twin-anode X-ray source XR50 of Mg/Al (1253 eV/1487 eV) operating at 150 W, placed perpendicular to the analyzer axis, and using a Phoibos 150 MCD-9 XP detector. The X-ray spot size was 650 μm. The pass energy was set to 25 and 0.1 eV for the survey and the narrow scans, respectively. Charge compensation was achieved with a combination of electron and argon ion flood guns. The energy and emission current of the electrons were 4 eV and 0.35 mA, respectively. For the argon gun, the energy and the emission current were 0 eV and 0.1 mA, respectively. The spectra were recorded with a pass energy of 25 eV in 0.1 eV steps at a pressure below 6 × 10⁻⁹ mbar. These standard conditions of charge compensation resulted in a negative but perfectly uniform static charge. The C1s peak was used as an internal reference with a binding energy of 284.8 eV. High-resolution XPS spectra were acquired by Gaussian-Lorentzian curve fitting after s-shape background subtraction. The surface composition was determined using the manufacturer's sensitivity factors.

Cell Cultures

MCF-7 and COS-1 cells were cultured in Dulbeccó's Modified Eagle's medium (DMEM) supplemented with 10% fetal bovine serum (FBS), 1% pen/strep and 2 mM L-glutamine. HUVEC cells were cultured in EGM-2 Bulletkit medium. The cells were cultured in 25 T-flask at 37 °C with 5% CO₂, 95% air and humid atmosphere. The cells of the culture that reached close to 90% confluence were detached using 0.05% trypsin/EDTA. Finally, cells were washed and re-suspended in a Ca²⁺-free culture medium to be counted and treated according to the procedures

Table 1 Characteristic FTIR bands of the species studied in this work

Compound		ν
ACP and cHAp	PO ₄ ³⁻ ν_1	962
	PO ₄ ³⁻ ν_3	1022, 1059, 1089
polyP	P-O-P symmetric stretching	734
	P-O-P asymmetric stretching	890
	PO ₃ ²⁻ vibrations	1100–1200
P ₂ O ₇ ⁴⁻	P-O-P symmetric stretching	736
	P-O-P asymmetric stretching	889
	PO ₃ ²⁻ vibrations	1100–1200
ATMP	P-O-CH ₂ stretching	1070
	Asymmetric vibrations of alkylphosphonic	939
	Symmetric vibrations of alkylphosphonic	1000
	P-C stretching	985

described below. The growth of the cells (i.e. during 48 h) in these Ca^{2+} -free media was performed as a control, being cell viability always greater than 95%.

Microinjection of Ca^{2+} and NPs Into Cells

MCF-7 and COS-1 cells were seeded onto glass cover slides of 0.8 cm diameter, which had previously been coated with 0.01% poly-L-lysine. Coating was performed overnight at 37 °C and under agitation. Cover slides were subsequently washed twice with PBS and absolute ethanol for sterilization. Finally, they were left in a laminar flow cabinet until the ethanol in excess was evaporated.

1.5×10^3 cells were seeded onto each cover slide and cultured during 24 h before being microinjected. This procedure allow that attached cells to resist the tensile stress that occur during the microinjection process. This was performed according to previously described procedures [24, 25]. Glass capillary (outer diameter of 2 mm) micropipettes (W-P Instruments, New Haven, CT) were prepared using a micropipette puller (PG-1, Narishige Scientific Instruments, Tokyo, Japan) that allowed getting a diameter of the tip close to 0.5–1.0 μm . After the capillary was pulled, the solution was delivered through its rear open end by means of a microloader (Eppendorf Microloader). The micropipette was then connected to the hub of the pipette holder, which was attached to the microinjector. Operations were done using a micromanipulator (Eppendorf 5171) and a microinjector (Eppendorf 5246) coupled with an inverted microscope (Olympus, Hamburg, Germany), which was equipped with phase-contrast and fluorescence optics. The temperature was maintained at 37 °C by using a plastic housing with an incubator (i.e. having supply of hot air and CO_2).

Microinjection was controlled using a tracer based on a loading buffer (4.8 mM K_2HPO_4 , 4.5 mM KH_2PO_4 , 14 mM NaH_2PO_4 at pH 7.4), solution of CaCl_2 and Texas red dextran (final concentration, 10 mg/mL) with M_w of 10,000 g/mol. The selected conjugate can remain in the microinjection place, while lower molecular weight conjugates (e.g. 3000 g/mol) can move from cytoplasm to the nucleus and vice-versa.

The tracer fluorescence (410–485 nm/515 nm, Ex/Em) was followed by taking images (1–10 min after microinjection). Suspensions of both kinds of NPs (i.e. < 200 nm and > 200 nm) were prepared using the same loading buffer.

Ca^{2+} Imaging Using Fura-2

Ca^{2+} -free, NPs < 200 nm and NPs > 200 nm were microinjected to obtain an intracellular Ca^{2+} concentration of 400 nM. The time-course of this Ca^{2+} was followed

with Fura-2 indicator. Specifically, the pipette was filled with 10 μL of the injection fluid having 1 mM Fura-2AM. Intracellular, unspecific esterases transform the acetoxymethyl ester (AM) to formaldehyde and acetic acid, which leads to the liberation of the Ca^{2+} indicator (i.e. Fura-2). The measurements of Fura-2 were carried out in an Olympus I \times 81 motorized inverted microscope (Olympus, Hamburg, Germany) controlled by Cell^{AM} software (Olympus Soft Imaging Solution). Fura-2 was alternately excited at 340 and 380 nm every 3 min and the emitted fluorescence was detected at > 500 nm. The changes of Fura-2 fluorescence were analyzed with the Cell^{AM} software.

Analysis of Surface Blebs

Microinjections were performed as described above. Ca^{2+} -free, NPs < 200 nm and NPs > 200 nm were microinjected to obtain intracellular Ca^{2+} concentrations of: 0, 100, 200, 400 and 800 nM. After 24 h of culture, images of the injected cells were taken by phase contrast microscopy and the percentage of the blebs surface was calculated on the basis of the total surface of the cells. Blebbing of the plasma membrane is a typical feature of cells undergoing late stage of apoptosis and is usually evaluated through the visible increase of the cytoplasmic diameter. Calculations were carried out by taking micrographs after microinjection at intervals of 1 min during 24 h and then during an additional period of 90 min to determine its stability. Time-lapse and images were analyzed using the EVOSTM software.

Electroporation of Ca^{2+} and NPs Into Cells

Electroporation was carried out using a BTX T820 square wave electroporator (BTX Harvard Apparatus). The electroporation parameters for each cell line were optimized for high electro-permeabilization and low cellular death. The cells were suspended in a pH 7 HEPES buffer (10 mM HEPES, 250 mM sucrose and 1 mM MgCl_2 in sterile water) at concentration of 6.1×10^6 cells/mL. Then, 270 μL of cell suspension (cooled at ~ 8 °C) were electroporated in presence of different concentrations of supplemented Ca^{2+} (i.e. 0, 0.025, 0.05, 0.1, 0.2, 0.4, 0.6, 0.8, 1.6 and 3.2 mM). Electroporations were carried out in cuvettes of 4 mm and using 8 pulses of 99 μs with 1.4 kV/cm and 1 Hz for MCF-7 cells, 1.2 kV/cm and 1 Hz for COS-1 cells, and 1.0 kV/cm and 1 Hz for HUVEC cells. These conditions depend on the cell type. The same procedure was performed for NPs < 200 nm and NPs > 200 nm. After electroporation, cells were washed two-times and resuspended in a Ca^{2+} -free medium. Then, cells were incubated at 37 °C and 5% CO_2 during 20 min. The protocol

was slightly changed when Ca^{2+} and NPs were chelated with EGTA. In these cases, cells were twice washed after electroporation and re-suspended in a Ca^{2+} -free medium supplemented with 0.5 mM EGTA-AM. Finally, they were washed in culture medium and diluted to be seeded in 96-well plates at a density of 10^4 cells/200 μL in each well. Assays were performed in triplicate at 24 h and 48 h of culture, the MTT and Alamar blue assays were selected to determine cell viability.

Loading of Ca^{2+} and ACP NPs Into Cells Without Electroporation

The cells after trypsinization were seeded in 96-well plates at a density of 10^4 cells/100 μL in each well. For this, a Ca^{2+} -free culture medium was used, and the plates were maintained under culture conditions for 24 h to allow cell adhesion. Then, 100 μL of the medium with 2X concentrations of Ca^{2+} were added to each well, to achieve the appropriate concentrations of Ca^{2+} (i.e. 0, 0.025, 0.05, 0.1, 0.2, 0.4, 0.6, 0.8, 1.6 and 3.2 mM). The same procedure was performed for NPs < 200 nm and NPs > 200 nm to obtain equivalent concentrations of Ca^{2+} despite being contained in the NPs. Each condition was tested in triplicate. At 24 h and 48 h of culture, the MTT and Alamar Blue assays were performed to determine cell viability using the CC_{50} value. The 50% cytotoxic concentration (CC_{50}) was defined as the Ca^{2+} concentration that reduced the cell viability by 50% when compared to untreated controls.

For the cases of Ca^{2+} and NPs chelated with EGTA, the cells after trypsinization were electroporated in the HEPES buffer supplemented with 0.5 mM EGTA-AM in the above described conditions. Subsequently, cells were incubated at 37 °C and 5% CO_2 during 20 min. Then, they were washed and diluted in a Ca^{2+} -free culture medium supplemented with 0.5 mM EGTA-AM to be seeded in 96-well plates at a density of 10^4 cells/100 μL in each well. After 24 h of culture, the medium was changed with 200 μL of fresh medium supplemented with 0.5 mM EGTA-AM and Ca^{2+} -free in different concentrations (i.e. 0, 0.025, 0.05, 0.1, 0.2, 0.4, 0.6, 0.8, 1.6 and 3.2 mM). The similar procedure was performed for NPs < 200 nm and NPs > 200 nm having the equivalent content of Ca^{2+} . Each condition was tested in triplicate at 24 h and 48 h of culture, being MTT and Alamar Blue assays were employed to determine cell viability.

MTT Viability Assay

Cell proliferation was evaluated using a filtered (through a 0.2 μm filter) MTT solution (1 mg/mL in phosphate buffer saline (PBS) of pH 7.4). Then, a mixture of 50 μL of MTT

and 200 μL of DMEM without phenol red were added into each well of a 96-well plate (except cell-free blank wells). The plate was incubated for 4 h under culture conditions. Finally, the MTT solution was removed and replaced with 200 μL of DMSO and 25 μL of Sorensen's glycine buffer (0.1 M glycine, 0.1 M NaCl, pH 10.5 after being adjusted with 0.1 M NaOH). The plate was maintained for 5 min at room temperature, and the optical density (OD) of each well was quantified by spectrophotometry using a plate reader (XMark™ Microplate Absorbance Spectrophotometer, Bio-Rad) at 570 nm.

Alamar Blue Viability Assay

The determination of metabolic activity using this assay is based on the mitochondrial hydrolase activity. The assay was performed according to the manufacturer's protocol. Cells were treated with 10% Alamar blue solution and kept at 37 °C for 2 h. Red fluorescence resulting from the reduction of Alamar blue was monitored (excitation/emission: 553/590) by spectrophotometry using a plate reader (XMark™ Microplate Absorbance Spectrophotometer, Bio-Rad).

Results and Discussion

Characterization of ACP

The morphology of ACP, which is displayed in Fig. 1a and b, reflect the influence of hydrothermal and aging conditions. ACP particles obtained using open aging, exhibit an pseudo-spherical morphology of nanometric dimensions. The average dimensions of ACP pseudo-spheres are displayed in Table 2.

Characterization of synthesized particles by X-ray diffraction (Fig. 1c) was focused on peaks at 2θ between 31.5° and 34.5°, which correspond to the (211), (112), and (300) hydroxyapatite reflections. The crystallinity and crystallite size determined for ACP samples are listed in Table 2.

Experimental Detection of Adsorption Onto ACP

The FTIR spectra of the synthesized ACP, polyP, $\text{P}_2\text{O}_7^{4-}$ and ATMP are displayed in Fig. 2a while the most characteristic bands of each compound are listed in Table 1. It should be noted that the asymmetric and symmetric stretching vibration of the P–O–P bridges are characteristic of polyP and $\text{P}_2\text{O}_7^{4-}$, even though they are not observed for ACP. The PO_3^{2-} vibration modes of polyP and $\text{P}_2\text{O}_7^{4-}$ are detected in 1000–1200 cm^{-1} domain, as detailed in

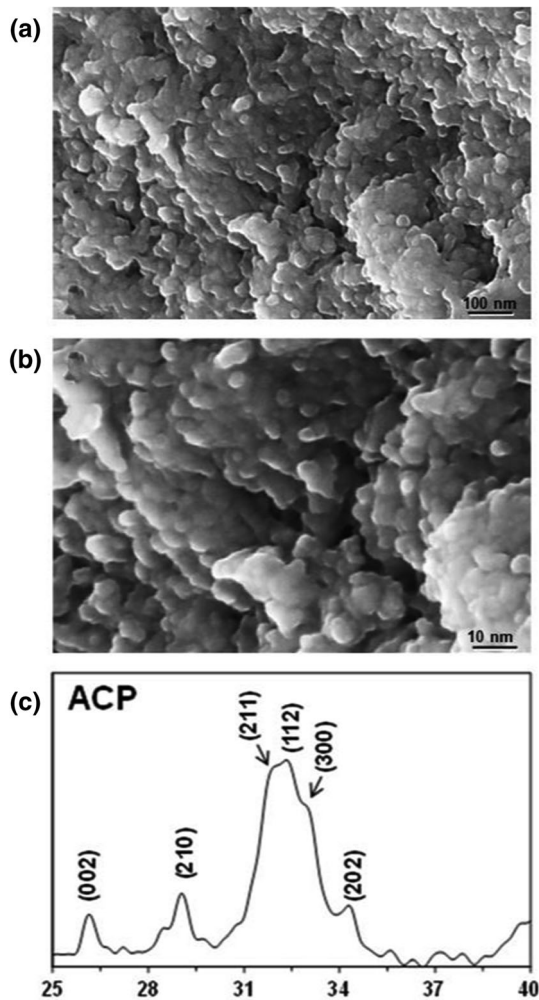


Fig. 1 Morphology and X-ray diffraction patterns of the ACP nanoparticles prepared in this work. **a** and **b** show low and high resolution SEM micrographs respectively. The hydroxyapatite was identified by the peaks at 33° – 34° 2θ

previous work [26]. On the other hand, the ATMP spectrum was recently described by some of us [27].

Figure 2b displays the FTIR spectra of ACP recorded after incubation in solutions which contained 12.5 mM of polyP, $P_2O_7^{4-}$ and ATMP at neutral pH. For polyP the characteristic absorption band is clearly identified at around 891 – 894 cm^{-1} . The band at 734 cm^{-1} is also detectable. Regarding the adsorption of $P_2O_7^{4-}$, a very weak shoulder associated to the band at 889 cm^{-1} is observed while, in opposition, the band at 736 cm^{-1}

remains practically undetectable. Although these results evidence the adsorption of polyP and $P_2O_7^{4-}$, difficulties in the identification of some characteristic bands suggest some limitations in such association processes. Finally the adsorption of ATMP, the shoulder detected at ~ 900 cm^{-1} transforms into a broad but weak band.

The ability of ACP to bind polyP and $P_2O_7^{4-}$ has been corroborated by XPS. Figure 2c represents the characteristic XPS spectra in the O1s region of ACP as prepared and after incubation in presence of polyP, $P_2O_7^{4-}$ and ATMP (all solutions at 12.5 mM). The sharp peak at 531.2 eV involve in all cases to the O1s of the PO_4^{3-} and OH^- groups of ACP [28]. The spectra of samples incubated in presence of polyP and $P_2O_7^{4-}$ show a shoulder at 533.3 eV, which corresponds to the oxygen atom involved in symmetric bridging P–O–P groups of the adsorbed molecules [29]. This result supports the adsorption previously detected by FTIR spectroscopy. Finally, the broad peak at 536.3 eV, which is only detected in samples with adsorbed polyP and $P_2O_7^{4-}$, can be attributed to non-bridging oxygen atoms [30], water accompanying the adsorbed compounds [31] or a combination of both.

Microinjection of ACP Into Living Cells

The intracellular effect of Ca^{2+} is still one of the most discussed aspects in the area of cellular physiology. This effect has relevant importance in the processes of cellular transfection, such as a non-viral transport of biomacromolecules. A typical intracellular level of Ca^{2+} is around 50–100 nM [32]. However, variations in cytosolic Ca^{2+} -free levels may be of great relevance in health. Transient increments in cytosolic Ca^{2+} concentration occur during the cell cycle (i.e. at the late G_1 prior to the initiation of the S phase and later on during G_2 before entry into M phase) [33, 34].

In the case of ACP nanoparticles uptake, a strong disturbance in cytosolic Ca^{2+} concentration may influence the progression of the cell cycle. A sharp increase in cytosolic Ca^{2+} concentration without any recovery can be associated with cell death. On the contrary, cells survived when they were able to decrease the cytosolic Ca^{2+} concentration to the baseline level [35]. In this study, we analyze the intracellular incorporation pathway of Ca^{2+} and calcium contained in the two amorphous calcium phosphate

Table 2 Physical parameters as determined by SEM and X-ray diffraction for ACP

	ACP
Average radius (R) and length (ℓ) of the observed nanostructures	$R = 2.6 \pm 0.2$ nm
Cristallinity (see Eq. 1)	$\chi_c = 3 \pm 1\%$
Crystallite size (see Eq. 2)	$L = 6 \pm 1$ nm

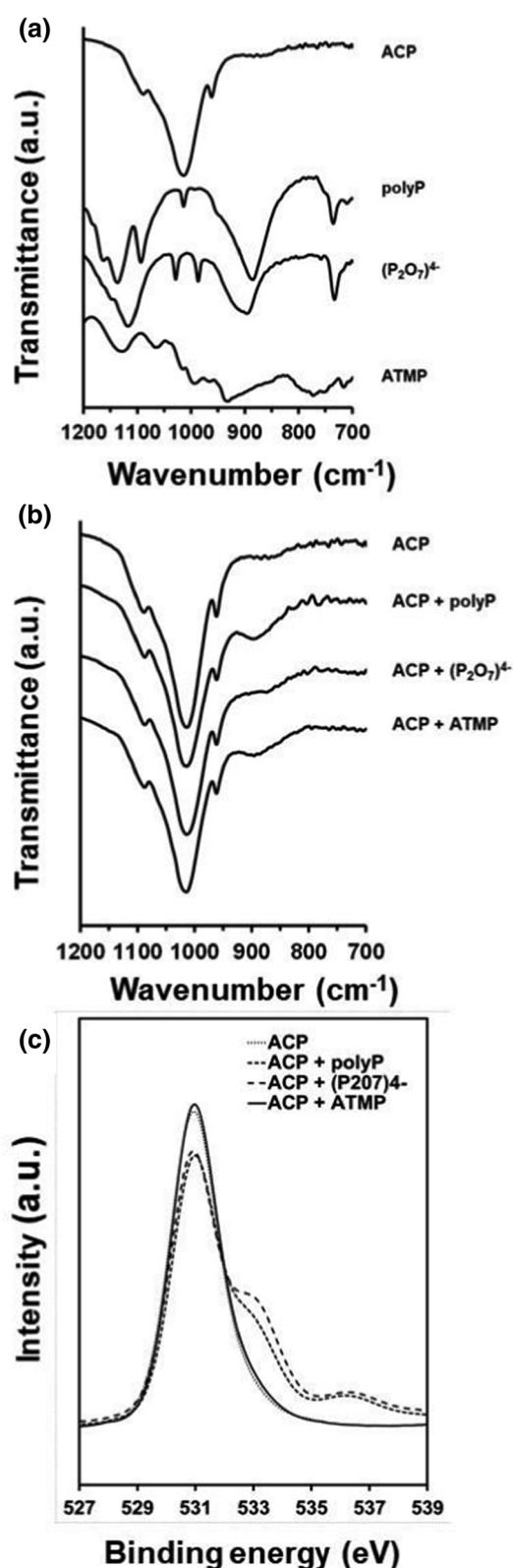


Fig. 2 FTIR and XPS spectra of the ACP nanoparticles prepared in this work **a** FTIR spectra of ACP, polyP, $P_2O_7^{4-}$ and ATMP; **b** FTIR spectra of ACP samples incubated in working aqueous solutions which contained 12.5 mM of polyP, $P_2O_7^{4-}$ and ATMP; and **c** High-resolution XPS spectra in the O1s region for ACP samples before and after incubation in presence of polyP (12.5 mM; top), $P_2O_7^{4-}$ (12.5 mM; middle) and ATMP (12.5 mM; bottom) at pH 7.4

nanoparticle fractions (i.e. NPs < 200 nm and NPs > 200 nm). Epithelial-type, fibroblast-type and endothelial-type cells (MCF-7, COS-1 and HUVEC cells, respectively) were considered to get more generalist conclusions.

The study was initiated with an analysis of the time-course of Ca^{2+} and NPs microinjected into the MCF-7, COS-1 and HUVEC cells to demonstrate unequivocally the direct effect of Ca^{2+} and NPs (Fig. 3a). For the microinjected Ca^{2+} (~ 400 nM), a progressive reduction of the intracellular Ca^{2+} concentration up to $\sim 50\%$ was observed after 24 h of its microinjection. On the contrary, for the microinjected NPs (equivalent to ~ 400 nM of Ca^{2+}), a rapid release of free Ca^{2+} was observed and corresponded to 100 nM (time 0 h, at the beginning of the experiment). These measurements were possible because the indicator Fura-2 is a ratiometric and sensitive dye for measuring intracellular Ca^{2+} . The time-course of Ca^{2+} contained in NPs showed a progressive increase in the intracellular Ca^{2+} concentration, demonstrating the occurrence of Ca^{2+} release from NPs injected into the cell cytoplasm. Thus, it was determined that after 24 h of the microinjection of NPs < 200 nm and NPs > 200 nm, the intracellular Ca^{2+} concentration was ~ 200 nM and ~ 150 nM, respectively (Fig. 3a). An observation that stands out from these pulse-chase experiments is the similar behavior of HUVEC, COS-1 and MCF-7 cells.

Analysis of Surface Blebs in Cells Incorporating ACP

On the other hand, the cytotoxic effect caused by different concentrations of Ca^{2+} and NPs were also evaluated (Fig. 3b). The cytotoxicity was followed by the formation of cytoplasmic blebs. For microinjected Ca^{2+} , a severe dose-dependent cytotoxic damage was observed. The highest microinjected dose (800 nM) caused a cell damage of 70–80% for the three cell types treated (i.e. HUVEC, COS-1 and MCF-7 cells). However, intracellular Ca^{2+} doses in the range of 100–400 nM shown a cytotoxic damage that was dependent on the cell type. Thus, endothelial HUVEC cells were the most sensitive (i.e. 40% of blebs) when the intermediate intracellular dose of 400 nM Ca^{2+} was applied. On the contrary, epithelial MCF-7 cells were less sensitive (i.e. 15% of blebs), while

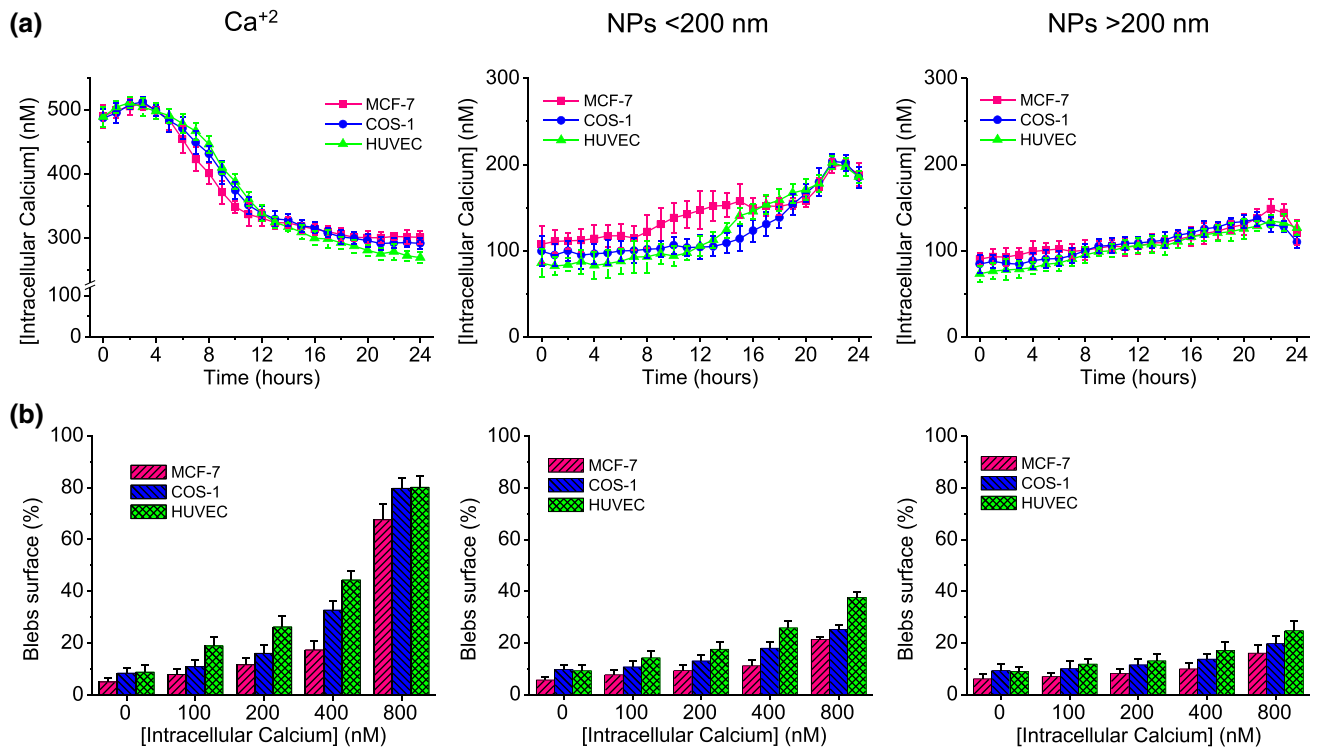


Fig. 3 Time-course and cytotoxic effect of the intracellular Ca²⁺, NPs < 200 nm and NPs > 200 nm microinjected into MCF-7, COS-1 and HUVEC cells. **a** Changes in cytoplasmic Ca²⁺ concentration after microinjection of 400 nM Ca²⁺ or their equivalent content in the case

of NPs. Ca²⁺ concentrations are relative to the control (physiological concentration ~ 100 nM). **b** Vesicular surface (blebs percentage) after microinjection of different concentrations of Ca²⁺ or their equivalent content in the case of NPs

COS-1 fibroblasts showed an intermediate cytotoxicity (i.e. 30% of blebs). A similar behavior was observed when NPs were microinjected, but the cytotoxic damage was smaller. Thus, the intracellular doses of NPs equivalent to 800 nM Ca²⁺ only produced a cellular damage close to 30–40% and 25–35% of blebs for the microinjection of NPs < 200 nm and NPs > 200 nm, respectively. This cytotoxic effect of the NPs was again related to the lower availability of Ca²⁺, since ions appear structured or bounded with the phosphate groups of the formed amorphous NPs.

Moreover, these results demonstrated the dependence of the cytotoxicity on the cellular type but more interestingly on their origin, or genetic condition. By contrast, HUVEC endothelial cells, which are derived from primary cultures and, therefore, can be considered normal, were the most sensitive to cytotoxic damage. Intermediate effect was observed with COS-1 fibroblasts, which are transformed cells by genetic modification, through the incorporation of SV40 particles.

Analysis of Cell Viability in Cells Incorporating ACP by Alamar Blue and MTT Assays

Figure 4 shows the viability results of cells exposed to different concentrations of Ca²⁺ and NPs. In these

experiments the cellular incorporation of Ca²⁺ was performed through a non-electroporation (-EP) diffusion process (Fig. 4a) and also by electrophoretic mobilization (i.e. electroporation (+ EP)) (Fig. 4b). The inhibition of the effect of Ca²⁺-free and Ca²⁺ released from NPs has been produced by its chelation using EGTA in both treatments (-EP and +EP). In these experiments are highly remarkable that the MCF-7 epithelial cells derived from adenocarcinoma were the most resistant to the cytotoxic effect of Ca²⁺.

Figure 4a clearly shows that during the -EP process the different concentrations of Ca²⁺-free and Ca²⁺ chelated with EGTA (in the range of 0–3.2 mM) have not effect on the viability of the three cell types (HUVEC, COS-1 and MCF-7). These results highlight that the entry of Ca²⁺ inside cells is an active transport through the cell membrane. Plasma membrane channels support the entry into cells of Ca²⁺ due to the gradient concentration driven process. Various calcium channels, such as voltage-gated Ca²⁺ channels (Ca_v family), can be involved in this Ca²⁺ influx. The expression of this family of proteins is a characteristic of “excitable cells” and these channels require depolarization of the plasma membrane for their activation [36].

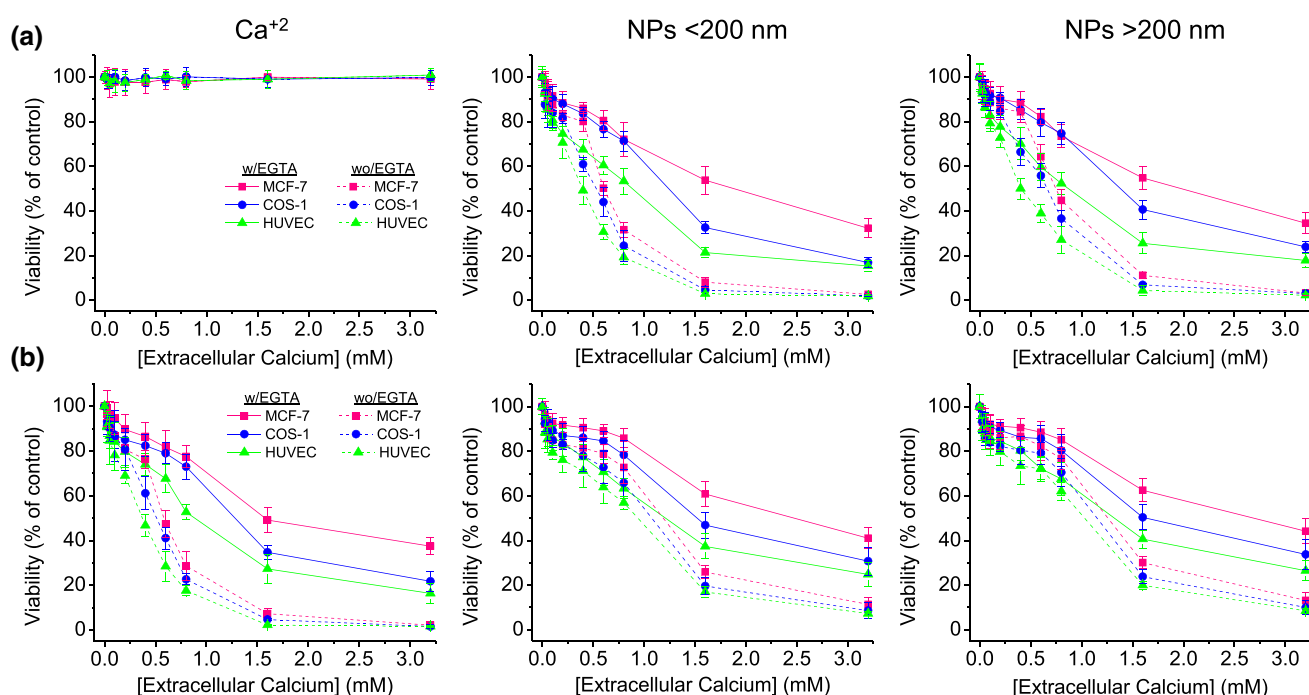


Fig. 4 Viability of MCF-7, COS-1 and HUVEC cells treated with extracellular Ca²⁺ and NPs < 200 nm and NPs > 200 nm by **a** non-electroporation (–EP) and **b** electroporation (+EP). Ca²⁺ concentrations in the range of 0 to 3.2 mM were considered in the presence and

absence of 0.5 mM EGTA as chelating agent. Cellular viability was measured with the Alamar Blue reagent after 24 h of culture

Despite Ca_v expression, Ca²⁺ entry in non-excitable cells mostly occurs through non-voltage gated channels. These include ligand-gated channels (e.g. P2X purinergic ionotropic receptor families), receptor-operated channels (ROC), secondary messenger-operated channels linked to GPCR activation, store-operated and stretch-operated channels. Numerous studies have shown that one or several Ca²⁺-permeable channels in the plasma membrane are modified in expression and/or activity in different cancer cells, and play a role in most of the pathophysiological processes driving the malignant phenotype. In addition to the plasma membrane Ca²⁺ channels, changes in Ca²⁺-transporters such as plasma membrane Ca²⁺-ATPase and Na⁺/Ca²⁺ exchanger have also been reported to be involved in the Ca²⁺ homeostasis of cancer cells and in tumorigenesis [37, 38]. Finally, it should be considered that the entry of Ca²⁺ ions into cells is a biological event regulated in a highly complex manner that does not depend exclusively on its gradient as can be seen in Fig. 4a for Ca²⁺-free experiments.

On the other hand, the forced incorporation of Ca²⁺-free by + EP (Fig. 4b) caused clear cytotoxic effects. The sensitivity of cells was in the order HUVEC > COS-1 > MCF-7 with CC₅₀ of 0.37, 0.51 and 0.58 mM, respectively (Table 3). In addition, this cytotoxic effect can clearly be inhibited when the Ca²⁺ was chelated, being logically the CC₅₀ values higher (i.e. 0.88, 1.27 and

1.56 mM for HUVEC, COS-1 and MCF-7, respectively) (Table 3). In this study, we have introduced EGTA-AM into cells, which became active after cleaving the acetoxymethyl ester (AM) by intracellular esterases. The released EGTA free acid was able to chelate intracellular Ca²⁺. Results about CC₅₀ changes were relevant and demonstrated the chelating effect of EGTA and that Ca²⁺ ions were responsible of triggering the cell death. The HUVEC endothelial cells were the most sensitive, followed by the COS-1 fibroblast cells, and finally by the MCF-7 epithelial cells.

However, both NPs < 200 nm and NPs > 200 nm showed similar dose–response effects under –EP conditions for viability of the different cell types. Figure 4a and Table 3 show that the CC₅₀ for the NPs < 200 nm were 0.40, 0.53 and 0.60 mM for HUVEC, COS-1 and MCF-7 cells, respectively. In addition, these CC₅₀ values increased to 0.88, 1.24 and 1.87 mM for HUVEC, COS-1 and MCF-7 cells, respectively, after Ca²⁺ chelation. A similar situation was observed for NPs > 200 nm with CC₅₀ values of 0.40, 0.65 and 0.75 mM, which after chelation increased to 0.83, 1.33 and 1.82 mM, for HUVEC, COS-1 and MCF-7 cells, respectively. These results suggest three clear features when the cells were exposed to NPs < 200 nm and NPs > 200 nm: (1) Similar cytotoxic effects were observed due to their ability to release Ca²⁺ into cells, being this effect inhibited by chelation with intracellular

Table 3 CC_{50} of Ca^{2+} and NPs incorporated into cells by electroporation (+EP) and non-electroporation (–EP). Experiments were performed with and without Ca^{2+} chelation (i.e. +EGTA and –EGTA, respectively)

Cell line	CC_{50} (mM)					
	Ca^{2+}		NPs < 200 nm		NPs > 200 nm	
	–EGTA	+EGTA	–EGTA	+EGTA	–EGTA	+EGTA
–EP						
MCF-7	–	–	0.60	1.87	0.75	1.82
COS-1	–	–	0.53	1.24	0.65	1.33
HUVEC	–	–	0.40	0.88	0.40	0.83
+EP						
MCF-7	0.57	1.56	1.19	2.46	1.25	2.65
COS-1	0.51	1.27	1.07	1.51	1.15	1.60
HUVEC	0.37	0.88	0.94	1.22	1.02	1.32

EGTA; (2) The occurrence of these cytotoxic effects has as a prerequisite that the NPs were internalized into the cells. The endocytosis pathway seems the most plausible via for –EP treatment; and (3). The endothelial HUVEC cells and the epithelial MCF-7 cells were the most and the least sensitive, respectively.

CC_{50} values were higher under +EP conditions for both released and chelated Ca^{2+} (Fig. 4b and Table 3). Thus, the CC_{50} values for HUVEC, COS-1 and MCF-7 cells exposed to the NPs < 200 nm were 0.94, 1.07 and 1.19 mM, respectively, for the released Ca^{2+} , and 1.22, 1.51 and 2.46 for the chelated Ca^{2+} . Highly similar values were obtained when HUVEC, COS-1 and MCF-7 cells were exposed to NPs > 200 nm. In this case, the CC_{50} values were 1.02, 1.15 and 1.25 mM, respectively, for released Ca^{2+} , and 1.32, 1.60 and 2.65 mM for chelated Ca^{2+} . These higher CC_{50} values can be explained taking into account that +EP fluidizes the plasma membrane and allows increases in the mobility of NPs as consequence of their electrical charge. Therefore, NPs cannot form vesicles and, therefore, the release of Ca^{2+} becomes smaller and higher concentration of NPs is required to achieve the CC_{50} . In general, the cytotoxic effect caused by +EP is lower than the one produced by –EP. The incorporated NPs are not vesiculated and, consequently, cannot reach pathways such as vesicle fusion, fusion with lysosomes or other cellular compartments when electroporation was applied.

In this study, viability was evaluated by the cells metabolic activity through the conversion of Alamar blue reagent by mitochondrial NADPH-oxidoreductase enzymes of viable cells after 24 h of culture (Fig. 4). Similar results were attained after prolonging cell cultures for 48 h (Mat. Suppl., Figure S1 and Table S1). Additionally, cell viability was determined by the MTT reagent, which is based on the metabolic activity mediated by mitochondrial and lysosomal NADPH-dehydrogenases of the viable cells, after 24 h and 48 h of culture (Mat. Suppl., Figure S2, S3, S4 and Table S2, S3). Cell viability was

found to be similar by applying both methodologies. Finally, the cytotoxic damage caused by ACP NPs could be related to their disposition to release Ca^{2+} (e.g. from the endocytic vesicles via fusion with lysosomes and from the cytoplasmic aggregate via dissolution). The increase in intracellular concentration of Ca^{2+} produced cell injury through the mitochondrial damage (Fig. 5).

Analysis of Cell Viability in Cells Incorporating ACP Incubated in Presence of polyP, $P_2O_7^{4-}$ and ATMP by Alamar Blue and MTT Assays

Recently, we have prepared modified ACP nanoparticles by adsorption of polyphosphates (polyP), orthophosphate ($(P_2O_7)^{4-}$) and phosphonate (ATMP) [39]. These surface modifications of the ACP NPs had an influence on their different physical and chemical characteristics (e.g. solubility). Interestingly, these surface modifications of ACP NPs can be reversed in some cases after specific treatments as it has been explored in this work. Thus, treatment with alkaline phosphatase in the presence of Mg^{2+} as cofactor can eliminate the adsorbed coating of orthophosphate and polyphosphates [39, 40]. Figure 6 displays the SEM micrographs of these synthesized nanoparticles. In all the cases we may observe poor dispersion and subsequent aggregation. Although dispersed nanoparticles could be obtained using hydrothermal conditions (20 Torr and 150 degrees C), we use ACP because is the first precipitate when adding Ca^{2+} solutions to phosphate aqueous solutions in physiological conditions [41].

In general, NPs coated with polyP, ATMP and $(P_2O_7)^{4-}$ showed a similar behavior than NPs without modification when they were incorporated into the cells by –EP and +EP. Thus, HUVEC and MCF-7 cells were the most and least sensitive, respectively. In all cases, CC_{50} values were higher when the incorporation of the NPs was performed with +EP compared to –EP (Fig. 7a, Table 4). However, it is remarkable that the NPs with modified surfaces and

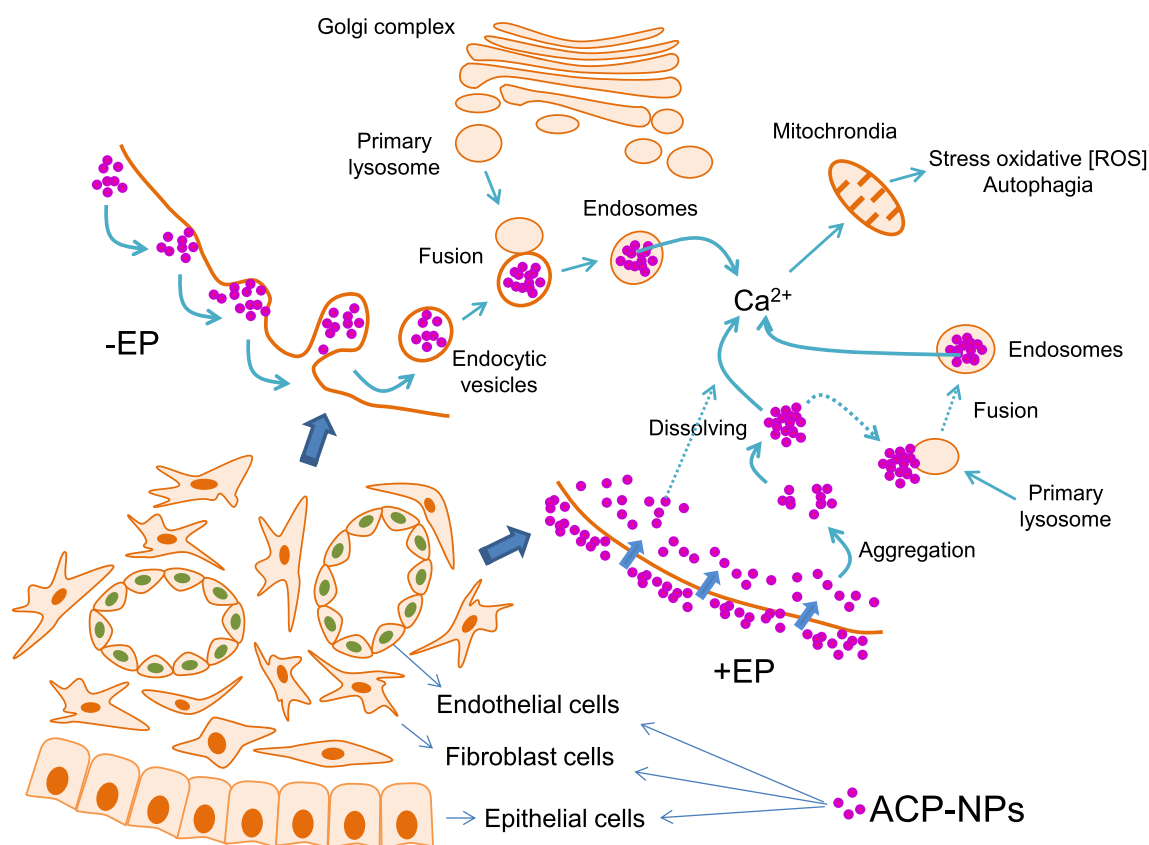


Fig. 5 Scheme of biological events relative to the cytotoxic effect of the intracellular Ca^{2+} , NPs < 200 nm and NPs > 200 nm microinjected into MCF-7, COS-1 and HUVEC cells

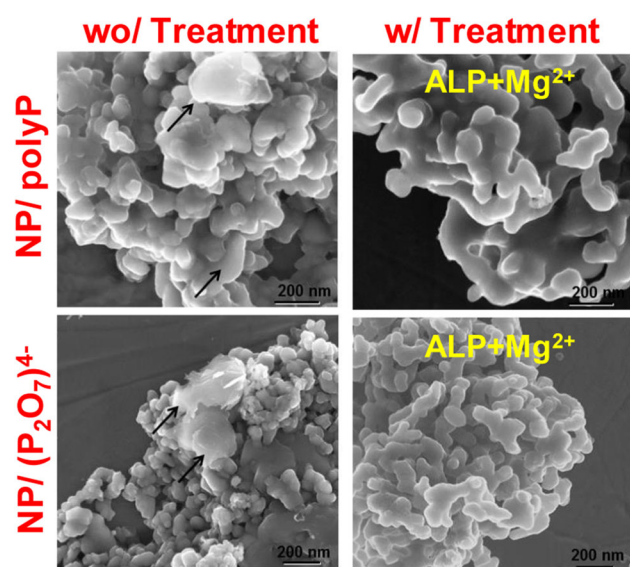


Fig. 6 Morphology of NPs modified by adsorption of biophosphates under SEM. Specific treatments with alkaline phosphatase (ALP) and Mg^{2+} as cofactor were applied to remove biophosphate coatings, respectively

incorporated by $-EP$ were less cytotoxic than NPs without modification. Thus, CC_{50} values of 0.85, 0.68 and

0.52 mM were determined for HUVEC cells treated with NPs coated with polyP, ATMP and $(\text{P}_2\text{O}_7)^{4-}$, respectively. By contrast, the CC_{50} values of NPs without surface modification were 0.39 mM. In addition, the same order of cell damage as a function of the coating ($\text{polyP} < \text{ATMP} < (\text{P}_2\text{O}_7)^{4-}$) was observed for COS-1 and MCF-7 cells with the $-EP$ treatment (Table 2). On the other hand, when the modified NPs were incorporated by $+EP$, the CC_{50} values were observed in the range of 1.0–1.3 mM without significant differences between the distinct NPs surface coatings (Table 2).

The treatment with alkaline phosphatase and the MgCl_2 cofactor of the superficially modified NPs resulted in a successful removal of polyP and $(\text{P}_2\text{O}_7)^{4-}$ modifications [42]. Thus, the CC_{50} values of NPs incorporated by $-EP$ were similar to the CC_{50} values of the unmodified NPs (e.g. CC_{50} values for HUVEC cells incorporating NP/polyP and NP/ $(\text{P}_2\text{O}_7)^{4-}$ were 0.43 and 0.42 mM, respectively (Table 4), which were close to the 0.39 mM value determined for NPs without surface modification). Note that these values were clearly lower than those obtained before the enzymatic treatment (i.e. 0.85 and 0.52 mM, respectively). In addition, this situation occurred in a similar way for MCF-7 and COS-1 cells (Fig. 7b and Table 4).

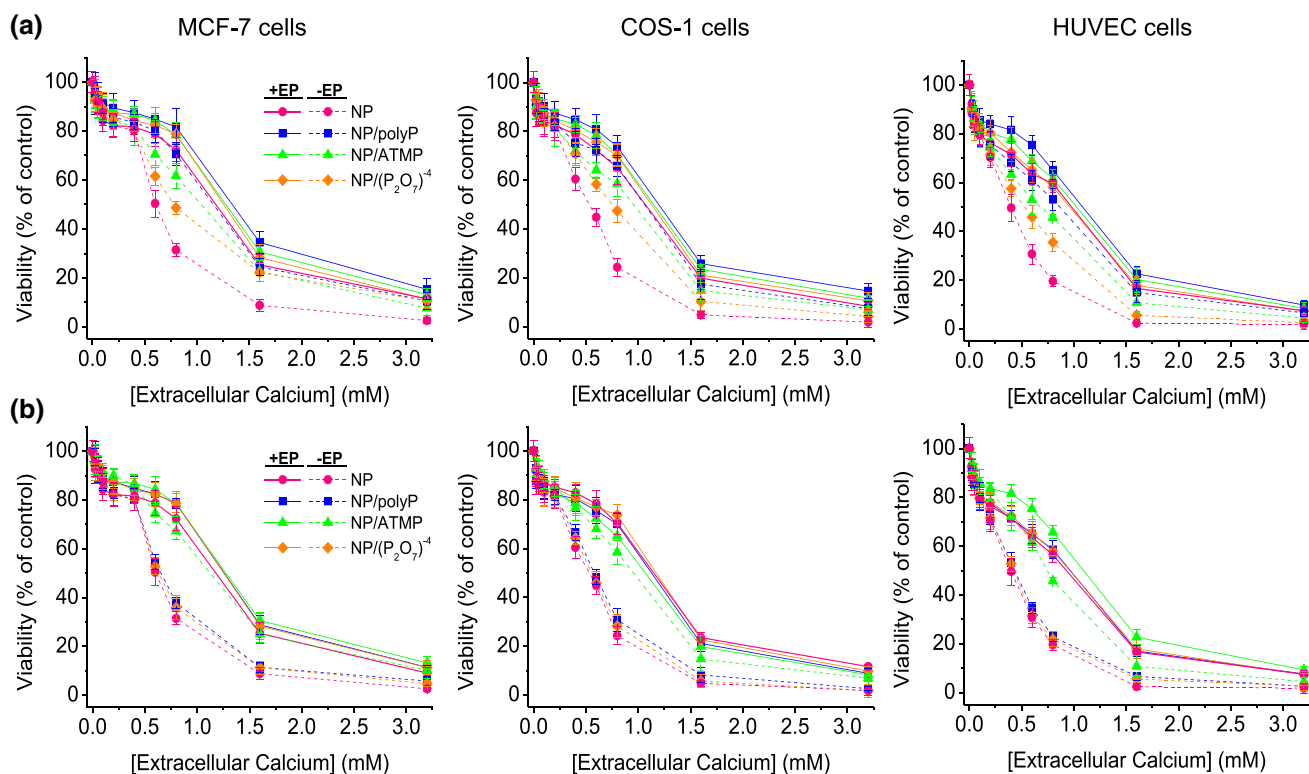


Fig. 7 Viability of MCF-7, COS-1 and HUVEC cells treated with NPs < 200 nm coated with biophosphates and biophosphonates. NPs with Ca^{2+} equivalent concentrations in the range of 0 to 3.2 mM were incorporated by non-electroporation (–EP) and electroporation

(+EP). Effect caused by coated NPs pre-treated with alkaline phosphatase alone (a) and together with Mg^{2+} as cofactor (b). The cellular viability was measured by Alamar Blue assay after 24 h of culture

Table 4 CC_{50} of NPs < 200 nm coated with biophosphates and phosphonates. NPs were incorporated into cells by electroporation (+EP) and non-electroporation (–EP). The effect was evaluated with and without any treatment

Nanoparticle	CC_{50} (mM)					
	MCF-7		COS-1		HUVEC	
	–EP	+EP	–EP	+EP	–EP	+EP
No-treatment						
NP	0.60	1.17	0.52	1.06	0.39	0.98
NP/polyP	1.15	1.34	1.06	1.20	0.85	1.08
NP/ATMP	1.03	1.28	0.95	1.15	0.68	1.02
$\text{NP}/(\text{P}_2\text{O}_7)^{4-}$	0.77	1.25	0.75	1.12	0.52	0.96
Treatment: ALP + MgCl_2						
NP	0.60	1.17	0.53	1.15	0.39	0.93
NP/polyP	0.66	1.26	0.58	1.13	0.43	0.96
NP/ATMP	1.13	1.28	0.95	1.06	0.74	1.10
$\text{NP}/(\text{P}_2\text{O}_7)^{4-}$	0.64	1.26	0.55	1.18	0.42	0.95

Finally, it is remarkable that the NPs incorporated by +EP and modified with the different coatings showed CC_{50} values with slight differences (e.g. see Table 4) after the enzymatic attack (Figures S5, S6 and Table S4). In summary, a constitutive and cumulative dissolution process took place and reached similar Ca^{2+} intracellular levels for all cell types. On the other hand, the endocytic pathway (–EP) of the different cell types demonstrates greater

differential sensitivity to NPs without or with surface modification. In any case, the ability to release its Ca^{2+} content and exert cell injury that ends in the death of cells is demonstrated.

Conclusions

Specific control of composition and size is one of the prime challenges in the synthesis of ACP, since such characteristics at the individual level determine the properties of the bulk dispersion and so the local damage in the living cell. ACP NPs have cytotoxic effects when internalized within cells. The endocytic pathway is more harmful than the incorporation by electroporation. The surface modification of ACP NPs and consequently the physical–chemical alteration (e.g. solubility decrease) of the NPs in subcellular compartments, such as lysosomes and mitochondria, decreased the severity of their cytotoxicity in the order polyphosphates < ATMP < orthophosphate. An interesting aspect that derives from this study is the differential cytotoxicity of the ACP NPs. Thus, it has been shown that epithelial-like MCF-7 cells were the most resistant to the effect of increased intracellular Ca²⁺ derived from ACP NPs, while endothelial-like HUVEC cells were the most sensitive and COS-1 cells fibroblasts-like showed an intermediate sensitivity. This result becomes significant if we consider the cellular organization of tissues as possible targets for treatment through the metabolic imbalance of calcium.

Supplementary Information The online version contains supplementary material available at <https://doi.org/10.1007/s10876-021-02182-6>.

Acknowledgements This work was supported by B. Braun Surgical S.A. through a joint research agreement with UPC, and by the MINECO/FEDER (MAT2015-69367-R and MAT2015-69547-R) and the Agència de Gestió d'Ajuts Universitaris i de Recerca (2017SGR359 and 2017SGR373). Support for the research of C.A. was received through the prize “ICREA Academia” for excellence in research funded by the Generalitat de Catalunya. This work is integrated within a wider research project supported by B. Braun Surgical S.A., UPC and ICFO and H. Germans Trias i Pujol.

Funding Open Access funding provided thanks to the CRUE-CSIC agreement with Springer Nature. This work was supported by B. Braun Surgical S.A. through a joint research agreement with UPC, and by the MINECO/FEDER (MAT2015-69367-R and MAT2015-69547-R) and the Agència de Gestió d'Ajuts Universitaris i de Recerca (2017SGR359 and 2017SGR373). Support for the research of C.A. was received through the prize “ICREA Academia” for excellence in research funded by the Generalitat de Catalunya. This work is integrated within a wider research project supported by B. Braun Surgical S.A., UPC and ICFO and H. Germans Trias i Pujol.

Availability of Data and Material The authors declare that all data supporting the findings of this study are available within the article file or from the corresponding author upon reasonable request.

Code Availability Not applicable.

Declarations

Conflict of interest Manuel Rivas Cañas declares that he has no conflict of interest. The authors certify that they have NO affiliations with or involvement in any organization or entity with any financial interest (such as honoraria; educational grants; participation in speakers' bureaus; membership, employment, consultancies, stock ownership, or other equity interest; and expert testimony or patent-licensing arrangements), or non-financial interest (such as personal or professional relationships, affiliations, knowledge or beliefs) in the subject matter or materials discussed in this manuscript.

Ethics Approval Not applicable.

Consent to Participate Not applicable.

Consent for Publication I, Manuel Rivas, give my consent for the publication of identifiable details, which can include photograph(s) and/or details within the text (“Material”) to be published in the above Journal and Article. I confirm that I have seen and been given the opportunity to read both the Material and the Article (as attached) to be published by Springer.

Open Access This article is licensed under a Creative Commons Attribution 4.0 International License, which permits use, sharing, adaptation, distribution and reproduction in any medium or format, as long as you give appropriate credit to the original author(s) and the source, provide a link to the Creative Commons licence, and indicate if changes were made. The images or other third party material in this article are included in the article's Creative Commons licence, unless indicated otherwise in a credit line to the material. If material is not included in the article's Creative Commons licence and your intended use is not permitted by statutory regulation or exceeds the permitted use, you will need to obtain permission directly from the copyright holder. To view a copy of this licence, visit <http://creativecommons.org/licenses/by/4.0/>.

References

1. M. J. Berridge, M. D. Bootman, and H. L. Roderick (2003). *Nat. Rev./Mol. Cell Biol.* **4**, 517. <https://doi.org/10.1038/nrm1155>.
2. T. Byers et al (2002). *CA* **52**, 92. <https://doi.org/10.3322/canjclin.52.2.92>.
3. M. L. McCullough, A. S. Robertson, C. Rodriguez, E. J. Jacobs, A. Chao, J. Carolyn, E. E. Calle, W. C. Willett, and M. J. Thun (2003). *Cancer Causes Control* **14** (1), 1. <https://doi.org/10.1023/a:1022591007673>.
4. M. C. Curry, A. A. Peters, P. A. Kenny, S. J. Roberts Thomson, and G. R. Monteit Monteit (2013). *Biochem. Biophys. Res. Commun.* **434**, 695. <https://doi.org/10.1016/j.bbrc.2013.04.015>.
5. V. Zaichick, S. Zaichick, and M. Rossmann (2016). *AIMS Mol. Sci.* **3** (4), 635. <https://doi.org/10.3934/molsci.2016.4.635>.
6. D. Clapham (2007). *Cell* **131**, 1047. <https://doi.org/10.1016/j.cell.2007.11.028>.
7. A. E. West (2001). *Proc. Natl. Acad. Sci. USA* **98**, 11024. <https://doi.org/10.1073/pnas.191352298>.
8. L. Contreras (2010). *Biochim. Biophys. Acta* **1797**, 607. <https://doi.org/10.1016/j.bbabi.2010.05.005>.
9. Z. Saidak (2009). *Endocrinol. Rev.* **30**, 1787. <https://doi.org/10.1210/er.2008-0041>.

10. D. G. Nicholls, S. L. Budd, and R. F. Castilho (1999). *Biochem. Soc. Symp.* **66**, 55. <https://doi.org/10.1042/bss0660055>.
11. P. S. Brookes, Y. Yoon, and S. S. Sheu (2004). *Am. J. Physiol. Cell Physiol.* **287**, C817. <https://doi.org/10.1152/ajpcell.00139.2004>.
12. P. Storz (2005). *Front. Biosci.* **10**, 1881. <https://doi.org/10.2741/1667>.
13. H. Pelicano (2004). *Drug Resist. Updates* **7**, 97. <https://doi.org/10.1016/j.drug.2004.01.004>.
14. H. Pelicano (2009). *Cancer Res.* **69**, 2375. <https://doi.org/10.1158/0008-5472.CAN-08-3359>.
15. N. Vanlangenakker and T. Vanden (2008). *Curr. Mol. Med.* **8**(3). <https://doi.org/10.2174/156652408784221306>.
16. S. Y. Proskuryakov and V. L. Gabai (2010). *Curr. Pharm. Des.* **16** (1), 56. <https://doi.org/10.2174/138161210789941793>.
17. R. A. Willis, *Pathology of tumours*, 4th ed. (Butterworths, London, 1967).
18. J. Folkman and R. Kerbel (2002). *Nat. Rev. Cancer* **2**, 717. <https://doi.org/10.1038/nrc905>.
19. J. Folkman (2003). *Semin. Cancer Biol.* **13**, 159. [https://doi.org/10.1016/s1044-579x\(02\)00133-5](https://doi.org/10.1016/s1044-579x(02)00133-5).
20. M. Rivas, L. J. del Valle, A. M. Rodriguez-Rivero, P. Turon, J. Puiggali, and C. Alemán (2018). *ACS Biomater. Sci. Eng.* **26**, 3234. <https://doi.org/10.1021/acsbiomaterials.8b00353>.
21. H. Klug and L. Alexander, *X-Ray Diffraction Procedure for Polycrystallite and Amorphous Materials*, 2nd ed. (John Wiley and Sons Press, New York, 1974).
22. E. Landi, A. Tampieri, G. Celotti, and S. Sprio (2000). *J. Eur. Ceram. Soc.* **20**, 2377. [https://doi.org/10.1016/S0955-2219\(00\)00154-0](https://doi.org/10.1016/S0955-2219(00)00154-0).
23. H. Orimo (2010). *J. Nippon Med. Sch.* **77**, 4. <https://doi.org/10.1272/jnms.77.4>.
24. W. Stockem, K. Weber, and J. Wehland (1978). *Cytobiologie* **70**, 2463.
25. P. P. Roger, F. Rickaert, G. Huezt, M. Authelet, F. Hofmann, and J. E. Dumont (1988). *FEBS Lett.* **232** (2), 409.
26. X. H. Guan, Q. Liu, G. H. Chen, and C. Shang (2005). *J. Colloid Interface Sci.* **289**, 319. <https://doi.org/10.1016/j.jcis.2004.08.041>.
27. V. Dalmoro, J. H. Z. dos Santos, E. Armelin, C. Alemán, and D. Azambuja (2013). *Appl. Surf. Sci.* **273**, 758. <https://doi.org/10.1016/j.apsusc.2013.02.131>.
28. X. L. Zhu, J. Chen, L. Scheideler, R. Reichl, and J. Geis-Gerstoefer (2004). *Biomaterials* **25**, 4087. <https://doi.org/10.1016/j.biomaterials.2003.11.011>.
29. W. Y. P. Y. Shih and T. S. Chin (1999). *J. Non-Cryst. Solids* **244**, 211. [https://doi.org/10.1016/S0955-2219\(00\)00113-0](https://doi.org/10.1016/S0955-2219(00)00113-0).
30. H. Goretzki, H. U. Chun, M. Sammet, and R. Bruckner (1980). *J. Non-Cryst. Solids* **42**, 49. [https://doi.org/10.1016/0022-3093\(80\)90007-1](https://doi.org/10.1016/0022-3093(80)90007-1).
31. C. S. K. Singamsetty, C. U. Pittman, G. L. Booth, G. R. He, and S. D. Gardner (1995). *Carbon* **33**, 587. [https://doi.org/10.1016/0008-6223\(94\)00144-O](https://doi.org/10.1016/0008-6223(94)00144-O).
32. S. Neumann (2009). *Biomaterials* **30**, 6794. <https://doi.org/10.1016/j.biomaterials.2009.08.043>.
33. J. T. Taylor, X. B. Zeng, J. E. Pottle, K. Lee, et al. (2008). *World J. Gastroenterol.* **14**, 4984. <https://doi.org/10.3748/wjg.14.4984>.
34. R. A. Steinhardt and J. Alderton (1988). *Nature* **332**, 364.
35. A. E. Ewence, M. Bootman, et al. (2008). *Circ. Res.* **103**. <https://doi.org/10.1161/CIRCRESAHA.108.181305>.
36. L. Kaestner, X. Wang, L. Herts, and I. Bernhard (2018). *Front. Physiol.* **9**, 450. <https://doi.org/10.3389/fphys.2018.00450>.
37. S. Marchi and P. Pintoni (2016). *Curr. Opin. Pharmacol.* **29**, 1. <https://doi.org/10.1016/j.coph.2016.03.002>.
38. V. Farfariello, O. Lamshanova, E. Germania, I. Fliniaux, and N. Prevarskaya (2015). *Biochem. Biophys. Acta* **1853** (9), 1974. <https://doi.org/10.1016/j.bbamcr.2015.03.005>.
39. M. Rivas, J. Casanovas, L. J. del Valle, O. Bertran, G. Revilla-López, P. Turon, J. Puiggali, and C. Alemán (2015). *Dalton Trans.* **44**, 9980. <https://doi.org/10.1039/C5DT00209E>.
40. L. Bloch-Frankenthal (1954). *Biochem. J.* **57** (1), 87. <https://doi.org/10.1042/bj0570087>.
41. E. D. Eanes, P. H. Gillesen, and A. S. Posner (1965). *Nature* **208**, 365.
42. M. Kunitz (1952). *J. Gen. Physiol.* **35** (3), 423. <https://doi.org/10.1085/jgp.35.3.423>.

Publisher's Note Springer Nature remains neutral with regard to jurisdictional claims in published maps and institutional affiliations.